

Design, Manufacturing, and Thermodynamic Analysis of a Gamma-type Stirling Engine Powered by Solar Energy

Tolga Topgül*

Gazi University, Department of Automotive Engineering, Turkey

In this study first a double-cylinder V-type air compressor has been converted to a gamma-type Stirling engine. Some components of the compressor have been used in the converted engine. For this reason, the air compressor has determined some technical features of the Stirling engine. Other parts of the Stirling engine have been manufactured. Then, the optimum operating parameters to provide maximum thermal efficiency have been investigated using the nodal thermodynamic analysis considering that the engine is powered by solar energy. In the analysis, helium as the working fluid is used due to its suitable thermodynamic features and safety usage. The optimum working fluid mass and engine speed have been determined as 0.15 g and 100 rad/s for all hot-end temperatures (750 K, 800 K, and 850 K). Also, the optimum displacer height has been determined as 190 mm since there is no significant improvement in the thermal efficiency after this dimension. The maximum thermal efficiency has been obtained as 46.5 % at 100 rad/s and 850 K. At this point, the indicated power is determined as 657.8 W. If the engine speed increases from 100 rad/s to 300 rad/s, the indicated power becomes 1141.5 W. The experimental results indicate that the maximum output power with helium is 42.5 W at 4 bar charge pressure, 260 rpm engine speed, and 350 °C hot-end temperature. The engine output power could be further increased with some modifications such as higher hot-end temperature, reduction of heat losses and gas leakage.

Keywords: γ -type Stirling engine, operating parameters, engine performance, thermal efficiency, nodal analysis

Highlights

- A double-cylinder V-type air compressor has been converted to a γ -type Stirling engine for use in solar energy applications.
- The structure of the air compressor has formed some parameters of the converted engine like phase angle, stroke, and cylinder diameter.
- The working fluid mass, engine speed, and displacer height have been optimized as operating parameters using the nodal thermodynamic analysis to obtain maximum thermal efficiency.
- According to the simulation results, the maximum thermal efficiency is 46.5 % and the maximum indicated power is 1141.5 W.
- The simulation results show that the thermal efficiency can be increased by optimizing the operating parameters.
- The experimental results indicate that the maximum output power with helium is 42.5 W at 4 bar charge pressure, 260 rpm engine speed, and 350 °C hot-end temperature.

0 INTRODUCTION

Stirling engines are external combustion engines. This feature eliminates the possible dependency of the engine on a specific energy resource and allows it to work with diverse energy sources, especially solar and other renewable energy sources. Also, Stirling engines could be built in different configurations that have a significant effect on the engine performance. With these aspects, Stirling engines have attracted the attention of researchers. In the Stirling engine studies, besides conventional energy sources, researchers around the world [1] to [5] consider environmentally friendly energy sources, such as biomass, solar energy, and waste heat. Also, there are many studies [6] to [9] on the configurations, driving mechanisms, and structural properties of the Stirling engines.

Air, helium, and hydrogen are usually used as the working fluid in the Stirling engines. Among the working fluids, helium and hydrogen come forward with their high heat transfer ability, which is important

for regenerative effectiveness, efficiency, and power. In fact, hydrogen can provide higher engine power than helium and other fluids; however, it has the risk of inflammation. For this reason, helium can be considered more advantageous [10] to [14].

The operating parameters and physical structure of the Stirling engine have a significant effect on its efficiency and performance. The effects of the operating parameters, drive mechanisms, and configurations of the Stirling engines on their performances can be seen in several studies in the literature. Cheng and Yang [15] performed a theoretical analysis on the performance of the kinematic types (α , β , and γ) of the Stirling engine. It was emphasized that the γ -type engine could operate at low-temperature differences compared to other kinematic Stirling engines, but it needed very effective mechanisms to provide sufficient output work.

Abuelyamen and Ben-Mansour [7] compared numerically three basic types of kinematic Stirling engines in terms of thermal efficiency and output

power. Their results showed that the highest thermal efficiency and output power were obtained with the γ -type engine as 9.8 % and 9.223 W, respectively. Also, the α -type engine had the lowest performance. Nevertheless, its performance was improved from 1.8 % and 0.908 W to 10.5 % and 9.856 W owing to the modification to have an annular connecting pipe instead of the circular pipe.

Laazaar and Boutammachte [2] investigated the suitable energy source for each Stirling engine type. For this purpose, they used the same physical and geometrical parameters in several kinematic types of Stirling engines by using a crank drive mechanism. They emphasized that each type of Stirling engine was more suitable for a particular energy to obtain high performance. The results of the study showed that the α -type engine was more applicable to waste heat recovery in the industrial sector owing to the high gas temperature, and the β and γ -type engines were more suitable for low and medium temperature differences like biomass and solar energy.

Topgül et al. [16] experimentally investigated the effect of the connection type (cold-end and hot-end) between the expansion and displacer cylinders on the output power and torque of a γ -type Stirling engine. It was observed that the engine performance improves with the hot-end connection compared with the cold-end connection at 30 °C cold and 200 °C hot source temperatures. The results showed that the maximum output power and engine torque for the hot-end connection were higher by 84.7 % and 68.4 % than those of the cold-end connection, respectively.

Kongtragool and Wongwises [17] emphasized the importance of dead volume and regenerator effectiveness. The results of the numerical simulation showed that decreasing regenerator effectiveness and increasing dead volume decrease the engine efficiency.

Cheng and Yu [13] researched the effect of the physical and geometric parameters on the thermal efficiency and performance of the β -type rhombic drive Stirling engine. For this purpose, the heat source temperature, offset distance between the crank and the center of the gear, regenerative gap, and distance between two gears were discussed in their parametric study. The results of the study showed that engine output power and efficiency could be improved by adjusting these parameters.

Ahmed et al. [18] performed the optimal design of a free piston β -type Stirling engine using a numerical model. According to the optimization results, about 7.95 kW engine power and 30 % thermal efficiency were obtained.

In a numerical study, Raghavendra et al. [19] investigated the effects of the operating and geometric parameters on the performance of a β -type Stirling engine. They expressed that as the displacer height was increased, both engine power and efficiency increased due to an increase in the compression ratio. The effects of the regenerator channel gap and offset distance from the crank to the center on the power and efficiency were similar. The results of the study indicated that the maximum engine power was 27.4 W at 1700 rpm and 800 °C.

Ahmed et al. [20] investigated the effects of the operating and geometric parameters on the performance of a β -type Stirling engine using a numerical model. The phase angle, temperature ratio, regenerator porosity, mean pressure, and frequency were optimized. The optimum value of the phase angle was found to be between 80° to 100° with regard to the engine efficiency and power. It was emphasized that the engine power decreased with the increasing temperature ratio and it decreased dramatically after the approximately 0.32 temperature ratio. They stated that the value of the frequency below 30 Hz was suitable for effective and efficient engine operation.

Aksoy et al. [21] experimentally investigated the performance of a β -type Stirling engine powered by solar energy. In the study, 400 W and 1000 W halogen lamps placed on the upper side of the displacer cylinder were used as the solar simulators. They obtained the hot-end temperatures as 623 K and 873 K for 400 W and 1000 W halogen lamps, respectively. They found that the maximum torque, power, and thermal efficiency with a 1000 W halogen lamp were 3.4 Nm, 127.17 W, and 12.85 %, respectively.

In a review study, Malik et al. [11] evaluated the applications and design parameters of the parabolic solar dish Stirling systems. They stated that a temperature level of 500 °C could be achieved with a parabolic trough collector, and 600 °C could be obtained using a parabolic solar dish collector. Additionally, they expressed that although the solar power tower had a higher temperature level (1000 °C), the parabolic solar dish systems would gain importance because of some disadvantages of the solar power tower. These disadvantages were mentioned by Cavallaro et al. [22] as higher greenhouse gas emissions (GHG/kWh), land use, and water usage. In another study, Sharma [23] emphasized that it could be achieved up to 600 °C using a parabolic trough or parabolic dish collectors in solar application systems. It was also expressed that the central tower was the most suitable solar power system for upper temperatures (more than 1000 °C).

In the present study, an air compressor that was produced for a different purpose was converted to an external combustion engine powered by eco-friendly energy sources. In the preliminary tests using LPG fueled heater, it was seen that the converted γ -type Stirling engine started to operate at low temperatures of approximately 100 °C using atmospheric air. This is promising for solar energy applications. The development of the engine and solar energy system has been proceeding. This study presents the manufacturing procedure and results of the thermodynamic analysis. Additionally, the pre-test results with air and helium are presented in this study and the experimental results are also compared to that of the nodal thermodynamic analysis.

1 MATERIAL AND METHODS

In this study, design, manufacturing, and nodal-thermodynamic analyses of a γ -type Stirling engine that can be used in solar energy applications were conducted. In terms of easiness of manufacturing, a V-type air compressor was converted to a γ -type Stirling engine by using the block, cylinders, connecting rods, and the crank mechanism of the compressor. In the theoretical analysis, the operating parameters were investigated for the designed and manufactured Stirling engine. In the analysis, the phase angle was used as 90° due to the structure of the V-type air compressor. This value is also suitable for Stirling engine applications in the literature [20]. In the numerical calculations, 750 K, 800 K, and 850 K hot-end temperatures were used considering the temperature range of the parabolic collector systems [11] and [23].

The system given as a schematic view in Fig. 1 could be considered for supplying solar power to the converted Stirling engine.

This application can be seen in some studies in the literature [11], [24] to [26]. It can be provided up to 600 °C (873 K) hot source temperature using the parabolic solar dish system as in Fig. 1 considering the literature [11] and [23]. This system using solar energy, an unlimited energy source can be defined as an eco-friendly power plant because of reducing the carbon footprint. Also, this system could be used to produce electricity [27] and [28].

1.1 Description of the Converted Stirling Engine

A γ -type Stirling engine was designed for solar energy applications. The photographs of the γ -type Stirling

engine converted from a V-type air compressor are seen in Figs. 2 and 3.

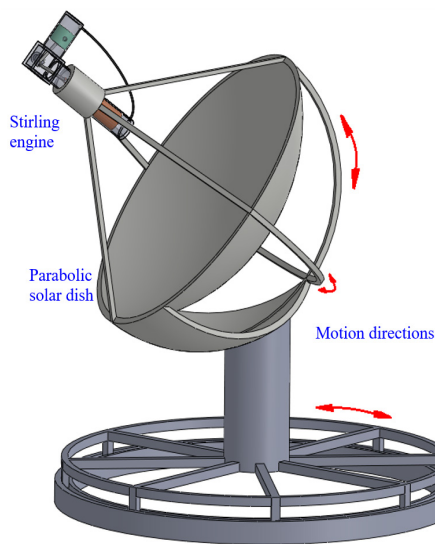


Fig. 1. The schematic view of the converted Stirling engine powered by solar energy



Fig. 2. The assembly photograph of the Stirling engine



Fig. 3. The top view of the engine

The air compressor's block, cylinders, connecting rods, and crank mechanism were used in the converted

Stirling engine seen in Figs. 2 and 3. Since the compressor had double cylinders, one of the cylinders formed the expansion cylinder which is also called the power cylinder, and the other formed the displacer cylinder. However, a new piston and cylinder head were required for the expansion cylinder. A new piston having the same diameter was manufactured from aluminum alloy. The material of the cylinder head was ASTM steel.



Fig. 4. The inner surface of the displacer cylinder

To form the displacer cylinder, additional parts were manufactured. For this purpose, a displacer cylinder, a displacer, and a displacer rod were manufactured. The displacer and its cylinder were manufactured from ASTM steel and the cylinder's

inner surface was enlarged with rectangular slots (see Fig. 4). The displacer cylinder was placed on the compressor cylinder using bolts. The connecting rods of the piston and displacer were connected to the same crankpin journal. The strokes of the piston and displacer and the angle between the cylinders were not changed because the air compressor's block and crank mechanism were used. For this reason, the phase angle between the cylinders was obtained as 90° . The expansion and displacer cylinders were combined via a hot-end connection. The advantages of the hot-end connection in the Stirling engines were previously presented by Topgül et al. [16] and Kentfield [29].

1.2 Principal of the Operation of the Converted Stirling Engine

P-V (pressure-volume) and T-s (temperature-entropy) diagrams and the positions of the converted γ -type Stirling engine during the cycle are given in Fig. 5. As shown in the figure, the engine turns anticlockwise. During the 1-2 process in which the crankshaft moves from -45° to 45° crankshaft angle (CA), the piston in the expansion cylinder goes from the top dead center (TDC) to the bottom dead center (BDC), the working fluid expands isothermally, and the piston produces work. The displacer is almost constant around the BDC.

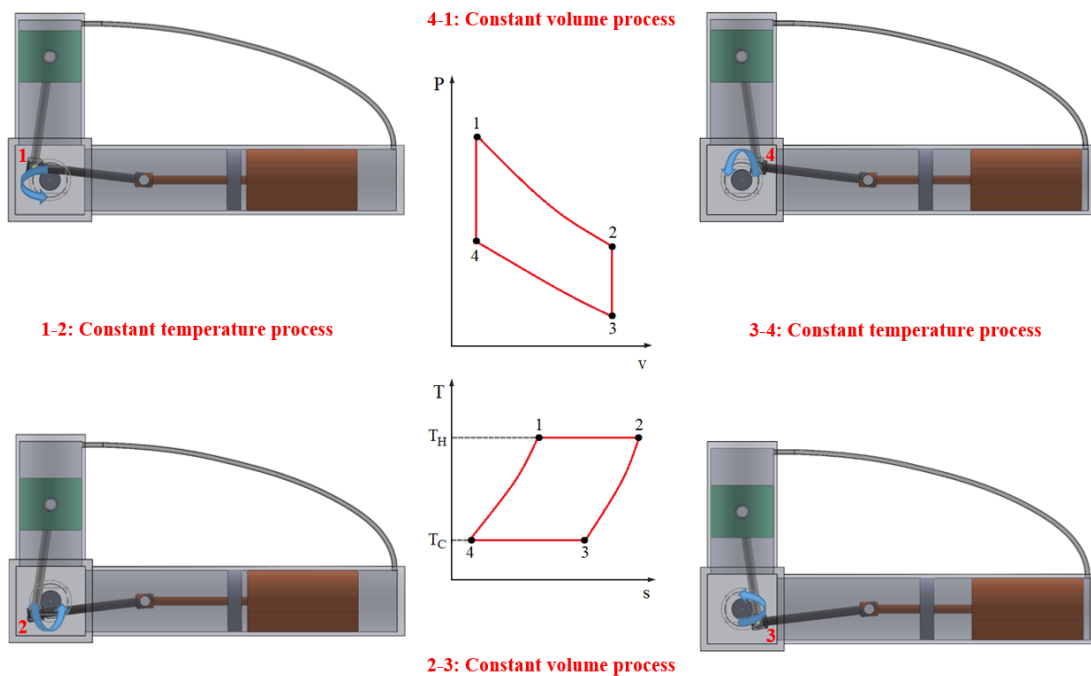


Fig. 5. P-V and T-s diagrams and the positions of the converted γ -type Stirling engine during the cycle

During the 2-3 process in which the crankshaft moves from 45° to 135° CA, the piston is almost constant around the BDC. The displacer goes from the BDC to the TDC, the working fluid passes through the heating-cooling channel between the cylinder wall and displacer from the hot volume to the cold volume. The hot volume decreases while the cold volume increases, because of this, the total volume does not change. At this constant volume process, the working fluid is cooled.

During the 3-4 process in which the crankshaft moves from 135° to 225° CA, the piston goes from the BDC to the TDC and the working fluid is compressed isothermally. During this process, the position of the displacer is almost near the TDC.

Finally, during the 4-1 process in which the crankshaft moves from 225° to 315° CA, the position of the piston is almost near the TDC. The displacer goes from the TDC to the BDC, the working fluid passes through the heating-cooling channel between the cylinder wall and displacer from the cold volume to the hot volume. The total volume does not change since the cold volume decreases while the hot volume increases. The working fluid is heated during this constant volume process. At the end of this process, the cycle is completed.

The variations in the volumes during the cycle are given in Fig. 6. As demonstrated in the figure, the phase angle between the expansion and displacer cylinders is 90° . Also, the total volume is the sum of the cold, hot, and expansion volumes.

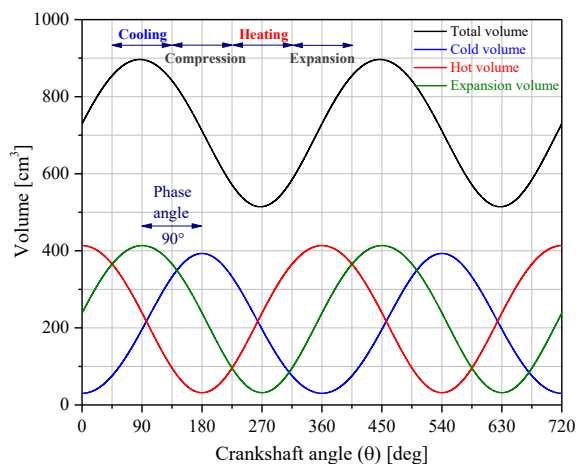


Fig. 6. The variations in the volumes with respect to the crankshaft angle

1.3 Mathematical Model

In the analysis, helium was chosen as the working fluid due to its suitable thermodynamic features and safety usage. In the literature, Cinar et al. [30] suggested in their experimental study to use as possible as high hot source temperatures and helium or hydrogen as the working fluid to improve engine performance. In a theoretical study, Chahartaghi and Sheykhi [31] expressed that the maximum engine power for helium was 5151 W at 1500 rpm and that of hydrogen was 12679 W at 3000 rpm. They stated that this was due to the viscosity of hydrogen being lower than that of helium. Also, it was emphasized that the higher specific heat value of hydrogen than that of helium affects the difference between the working fluid temperature and the wall temperatures. Ben-Mansour et al. [32] used air, helium, and hydrogen as working fluids. Hydrogen, which is among the working fluids used, possesses the highest thermal conductivity, while air has the lowest. They stated that this feature affects heat transfer and absorption amount of heat. Shufat et al. [28] and Cheng et al. [33] reported that engine power is much higher when using helium as a working fluid compared to air. Ahmet et al. [18] proposed helium as the working fluid for Stirling engines since hydrogen has a low molar mass, reactive nature, and inflammatory properties.

In this study, the nodal analysis method was used for thermodynamic analysis. The simulation study was conducted on the γ -type Stirling engine considering similar studies in the literature [34] to [40]. The specifications of the engine and the simulation inputs are shown in Table 1.

The assumptions in the analysis were considered as follows:

1. The working fluid is an ideal gas.
2. There is no leakage, so the total mass of fluid in the total volume does not vary.
3. There are no pressure drops. The pressure of the working fluid in all of the nodal volumes is equal.
4. There is no heat transfer from the engine to the ambient.
5. There is no mechanical loss.
6. The rotational speed of the crankshaft does not vary for each thermodynamic solution.
7. The wall temperatures of the nodal volumes are constant and foreknown, as shown in Fig 7.
8. During the regeneration, the variation of the wall temperature between cold-end and hot-end temperatures is linear and does not change with time.

Table 1. The simulation inputs and the specifications of the converted γ -type Stirling engine

Working fluid	He	Helium
Gas constant of helium [J/(kgK)]	\mathfrak{R}	2077
The specific heat at constant pressure [J/(kgK)]	c_p	5192.6
The specific heat at constant volume [J/(kgK)]	c_v	3115.6
Compression ratio		1.74
Displacer diameter [mm]	D_d	88.5
Piston diameter [mm]	D_p	90
Displacer rod diameter [mm]	D_{dr}	20
Convective heat transfer coefficient in the cooler, regenerator, and heater [W/(m ² K)]	h	1200
Convective heat transfer coefficient in the cylinders [W/(m ² K)]	h_c	70
Displacer height [mm]	h_d	190
Distance between piston pin center and piston top [mm]	h_p	38
Engine speed [rad/s]	ω_e	100
Crank radius [mm]	R_c	30
Displacer rod length [mm]	R_{dr}	167.3
Connecting rod length [mm]	R_{cr}	180
Hot-end temperature [K]	T_H	750
		800
Cold-end temperature [K]	T_C	850
		350
Distance between the crankpin center and displacer cylinder bottom [mm]	Z_c	312.3
Distance between the crankpin center and expansion cylinder top [mm]	Z_e	253
Distance between the crankpin center and displacer cylinder top [mm]	Z_h	572.3

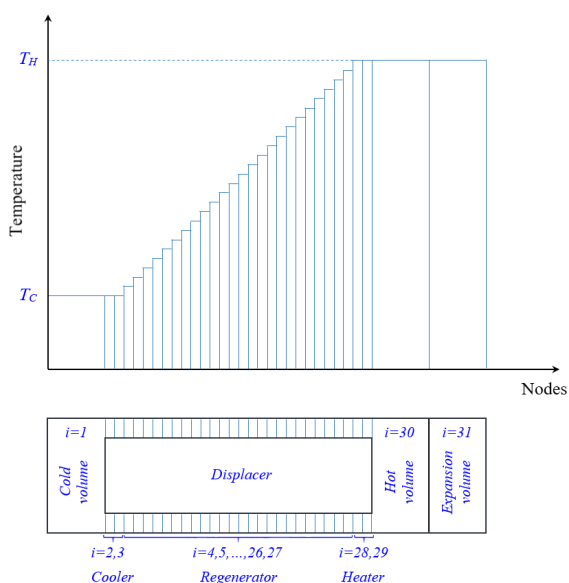


Fig. 7. The nodal volumes and wall temperature distribution

The working fluid in the Stirling engine continuously moves between the expansion and

displacer cylinders during the cycle. In other words, the working fluid passes through the cold volume, cooler, regenerator, heater, hot volume, and expansion volume. In the calculations, the total volume was divided into 31 nodal volumes. Fig. 7 depicts all nodal volumes used in the simulation and the boundary temperatures of the nodal volumes. The first nodal volume is the cold volume of the displacer cylinder and is indicated by $i = 1$. The cooler, regenerator, and heater volumes in the heating-cooling channel between the cylinder wall and displacer are indicated by $i = 2, 3, i = 4, 5, \dots, 27$, and $i = 28, 29$, respectively. The hot volume of the displacer cylinder is indicated by $i = 30$. The last of the nodal volumes, $i = 31$, is the expansion volume.

A schematic figure of the converted engine is indicated in Fig. 8. As indicated in Fig. 8, β_d specifies the angle between the axis of the displacer cylinder and the axis of the connecting rod of the displacer. β_d can be defined with respect to the crankshaft angle (θ).

$$\beta_d = \arcsin\left(\frac{R_c}{R_{cr}} \sin\theta\right), \quad (1)$$

where β_p specifies the angle between the axis of the expansion cylinder and the axis of the connecting rod of the piston (Fig. 8). β_p can be defined with respect to θ .

$$\beta_p = \arcsin\left(\frac{R_c}{R_{cr}} \cos\theta\right). \quad (2)$$

The cold, hot, and expansion volumes can be obtained using Eqs. (3) to (5), respectively.

$$V_1 = (-R_c \cos\theta + R_{cr} \cos\beta_d + R_{dr} - Z_c) \cdot (A_p - A_{dr}), \quad (3)$$

$$V_{30} = (Z_h - (-R_c \cos\theta + R_{cr} \cos\beta_d + R_{dr} + h_d)) \cdot A_p, \quad (4)$$

$$V_{31} = (Z_e - (-R_c \sin\theta + R_{cr} \cos\beta_p + h_p)) \cdot A_p. \quad (5)$$

The pressure can be determined using the Schmidt formula (Eq. (6)).

$$p = \frac{m\mathfrak{R}}{\sum_{i=1}^{31} \frac{V_i}{T_i}}. \quad (6)$$

The working fluid temperature in a nodal volume can be calculated via Eq. (7).

$$T = T^F + \Delta T. \quad (7)$$

In Eq. (7), the T^F indicates the working fluid temperature within the time step before the current one. ΔT , the temperature variation in the nodal volume

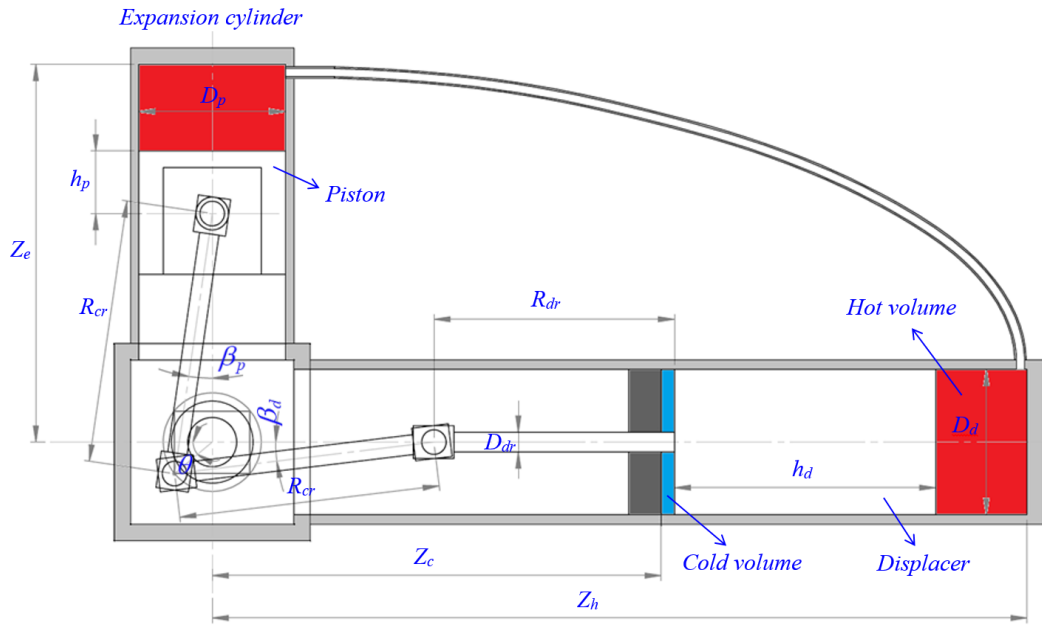


Fig. 8. The schematic figure of the converted γ -type Stirling engine

within the time step, can be defined via the first law of thermodynamics (Eq. (8)).

$$\Delta Q - \Delta W = H_o - H_i + (\Delta U), \quad (8)$$

where ΔQ is the heat exchange between the working fluid and the nodal volume, ΔW is the work generated in the nodal volume, ΔU is the variation of the internal energy in the nodal volume, H_o is the enthalpy of the outgoing working fluid from the nodal volume, and H_i is the enthalpy of the entering working fluid into the nodal volume.

1.4 Results of the Pre-Test and Comparison with Nodal Thermodynamic Analysis Results

The converted Stirling engine is tested in an experimental setup as seen in Fig. 9. In the experiments, the hot-end temperature was set at $350 \pm 5 \text{ }^\circ\text{C}$ by using an LPG-fueled heater. The cold-end temperature was adjusted to $35 \pm 2 \text{ }^\circ\text{C}$ by circulating the cooling water into the water jacket. All temperatures were measured NiCr-Ni thermocouples and a 12-channel Elimko 6000 brand device. The working fluid pressure was measured with a burdon tube manometer. To impose variable loading conditions on the engine used a prony-type dynamometer. The ESIT BB20 brand load cell was also used to determine brake torque. Finally, the measurement of the engine speed was performed via ENDA ETS1410 digital tachometer.

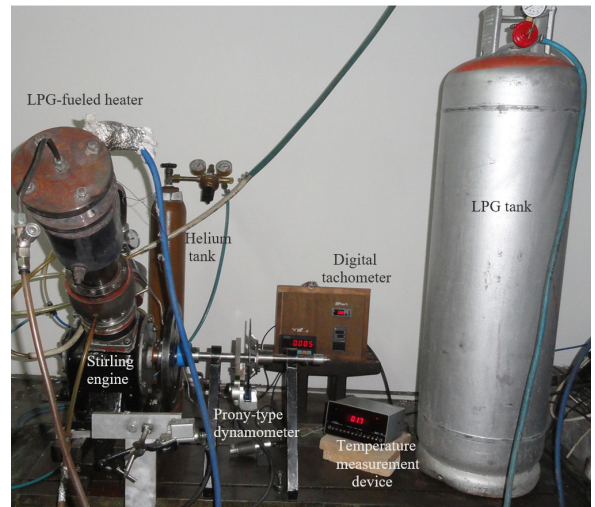


Fig. 9. The photograph of the experimental setup

Table 2. The accuracies of the measurement equipment and the uncertainty of the calculated value

Measured values	Accuracy
Temperature	$\pm 1 \text{ }^\circ\text{C}$
Gauge pressure	$\pm 0.1 \text{ bar}$
Torque	$\pm 0.003 \text{ Nm}$
Speed	$\pm 1 \text{ rpm}$
Calculated value	Uncertainty
Engine output power	0.4 % to 2.85 %

It can be seen in Table 2, the accuracies of the measurement equipment and the uncertainty of the

calculated parameter. Similar to the experimental studies in the literature [16], [41] to [44], the route mean square method was used for uncertainty analysis. Additionally, the error bars based on the accuracies of the measurement equipment and the maximum uncertainty are used in Fig. 10 similar to the literature [16] and [45]. Some of the error bars may not be noticed due to their small values or scale.

Fig. 10 shows the comparison of the engine output power obtained with air and helium at different charge pressures. The charge pressure is given as the absolute pressure in this figure. Compared to the air, helium had a higher improvement in the engine power for all charge pressures. While the maximum engine power with air was obtained as 9.8 W at 123 rpm engine speed and 3 bar charge pressure, helium provided significantly higher power at higher engine speed and charge pressure (42.5 W at 260 rpm and 4 bar). This result agrees with the literature [28], [30], [32], and [33]. However, the output power decreased when the charge pressure was increased more for both working fluids.

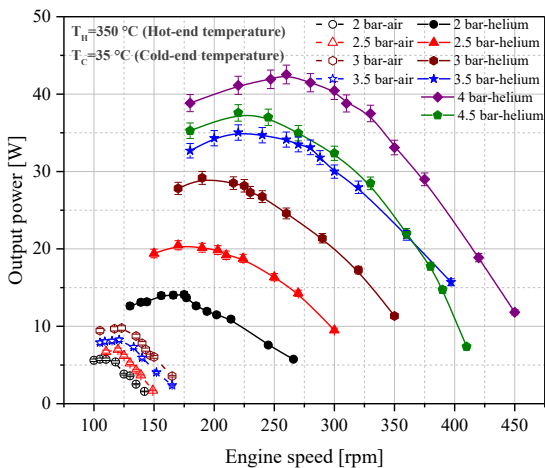


Fig. 10. The variation of the engine output power at different charge pressures with air and helium

Fig. 11a depicts a comparison of the experimental and theoretical analysis results for helium at the charge pressures of 2.5 bar and 4 bar. While the experimental results expressed the engine output power, the results of the nodal thermodynamic analysis stated the indicated engine power in ideal operating conditions such as using ideal gas, no leakage, no pressure drops, etc. The assumptions in the analysis are given in Section 1.3.

The maximum output power values were found as 20.5 W and 42.5 W at 2.5 bar and 4 bar charge pressure, respectively. At the points corresponding to

these values, the values of the indicated power were determined as 77.1 W and 188.9 W, respectively. The differences in these values result from comparison with the indicated power and effective power (engine output power). The friction may also have some influence on this difference. Since the friction depends on the engine speed, higher difference appears at high speeds. In the theoretical analysis, the factor limiting the power is the engine speed which shortens the time required for adequate heat transfer. For this reason, the maximum indicated power could be obtained at a higher engine speed. However, this engine speed was not reached in the pre-tests. For all these reasons, as seen in Fig. 11a, the difference between theoretical and experimental results increases with the increase in the engine speed. Fig. 11b shows the extended scale of the engine speed. Theoretically, as illustrated in this figure, the maximum indicated power is obtained as 573 W at 2.5 bar charge pressure and 2387 rpm engine speed, while it is 571.5 W at 4 bar and 1432 rpm.

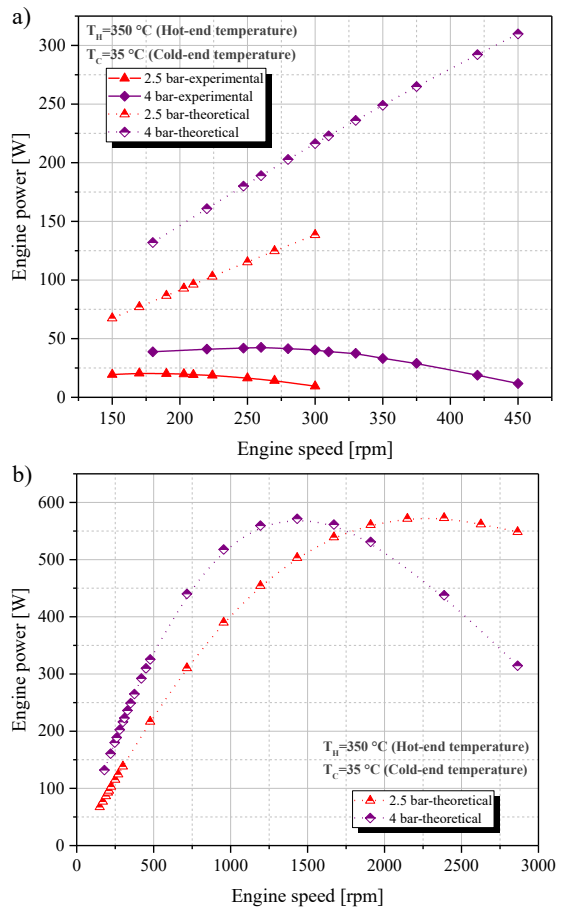


Fig. 11. a) The comparison with experimental and theoretical results; and b) the variation of the theoretical results versus engine speed

The results of the theoretical analysis show the highest achievable engine power. In other words, it shows the upper limit of engine performance under the considered operating conditions. In practice, this limit can be reached as the engine and operating conditions become perfect. Some improvements can be performed by reducing heat losses, friction losses, and pressure losses, or increasing regeneration effectiveness and providing sealing. To obtain more power, the Stirling engine should be operated at a higher engine speed with the best regenerator effectiveness.

2 RESULTS AND DISCUSSION

The phase angle, cylinder diameter, stroke, displacer height, engine speed, hot source temperature, cold source temperature, etc. are some operating and structural parameters in a Stirling engine. These parameters, which have a significant impact on engine performance, need to be evaluated according to the configuration of the Stirling engine. The γ -type Stirling engine was converted from a V-type air compressor and optimized to operate with the highest efficiency in solar energy applications. For this reason, this study aimed to maximize the thermal efficiency by optimizing the hot-end temperature, the mass of the working fluid, engine speed, and displacer height. In the analysis, the hot-end temperature range was determined considering parabolic collector systems.

2.1 The Effect of Working Fluid Mass

The effect of the working fluid mass and hot-end temperature on the engine efficiency and power is given in Fig. 12. These simulation results are compatible with the literature [18], [34], [35], [46], and [47].

As indicated in the figure, the highest engine power and thermal efficiency are obtained at 850 K hot-end temperature. Compared with their maximum values at 750 K, the thermal efficiency and the engine power at 850 K were improved by 14 % and 44 %, respectively. Considering the effect of the working fluid mass, it can be seen that the thermal efficiency increases up to its maximum value at 0.15 g for all hot-end temperatures as the mass increases. The low mass value means that the amount of the working fluid in the circulation is low. For the heating-cooling process, it is needed that enough working fluid circulates between cold and hot volumes. For this reason, the thermal efficiency at the lower mass of the working fluid was relatively low compared to

that of 0.15 g. Also, charge pressure which figures the cyclic average pressure is lower due to the low mass of working fluid. As illustrated in Fig. 13, charge pressure which expresses the produced amount of the indicated work increases depending on the mass of the working fluid. For maximum thermal efficiency, the optimum working fluid mass was determined as 0.15 g. With the increase in the mass of the working fluid above this value, the thermal efficiency decreased due to inadequate heat transfer to the working fluid. It means that the capacities of the heating-cooling processes are inadequate for working fluid mass. In this study, an external heater-cooler and a regenerator were not used. It was assumed that the heat transfer occurs from the surfaces of the cylinders. For this purpose, the inner surface of the displacer cylinder was enlarged with rectangular slots. It can be used as an external heat exchanger to increase heat transfer.

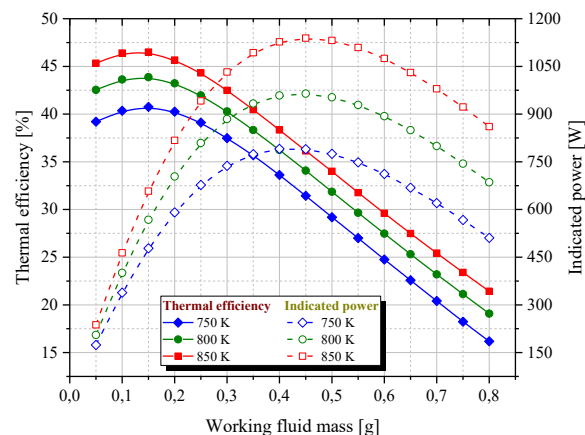


Fig. 12. The effect of the working fluid mass on the indicated power and thermal efficiency

The engine power showed a similar inclination with the thermal efficiency, but its maximum value was obtained at about 0.45 g mass of working fluid. The power depends on the work per cycle. For this reason, the power increased as the work increased. The area shown in the pressure-volume (P-V) diagram indicates the work of the cycle (see Fig. 13). As shown in the figure, the indicated work at 0.45 g is higher than that of the 0.15 g mass of working fluid at all hot-end temperatures. However, as seen in the figure, the indicated work is close to the isothermal work at 0.15 g because of the higher thermal efficiency.

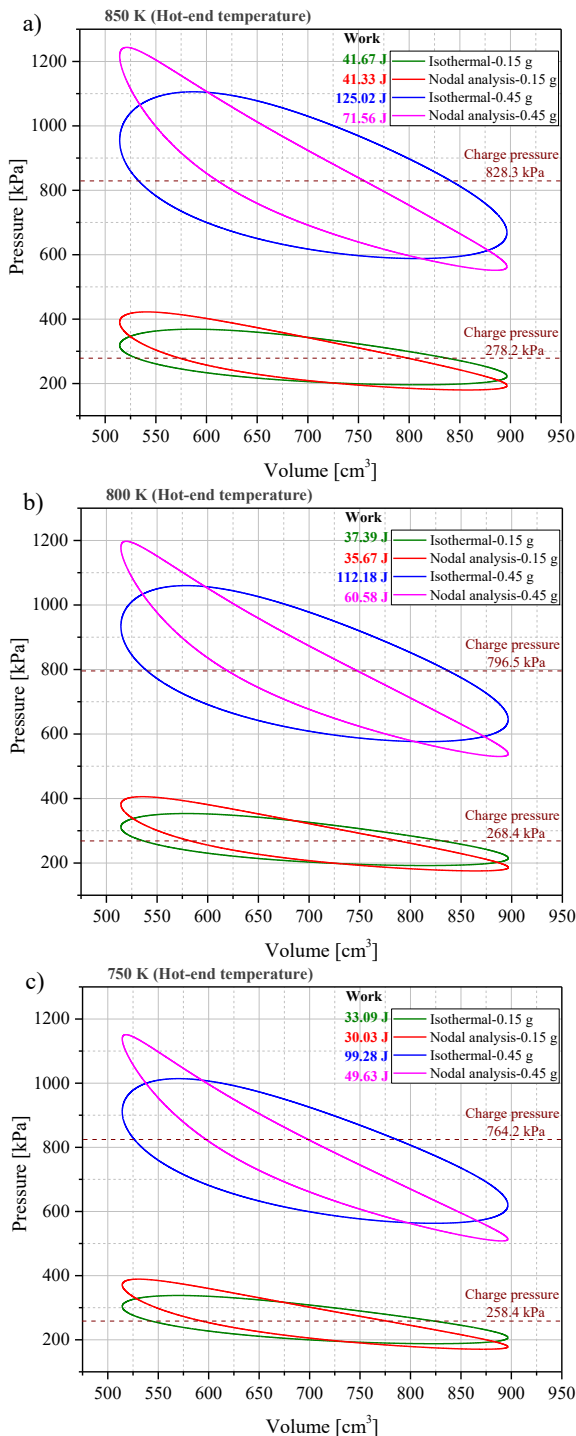


Fig. 13. The effect of the working fluid mass on the P-V diagram at hot-end temperatures; a) 850 K, b) 800 K, and c) 750 K

2.2 The Effect of Engine Speed

The effect of the engine speed on the indicated power and thermal efficiency is seen in Fig. 14. At low

engine speeds, the thermal efficiency was relatively low. The reason for this may be inadequate working fluid mass in the circulation. Also, the indicated engine power was considerably low up to 300 rad/s engine speed due to the lower number of cycles. However, the efficiency and power increased up to their maximum values depending on increasing the engine speed. The thermal efficiency and indicated power began to decrease over 100 rad/s and 300 rad/s, respectively. The working fluid has less time at higher engine speeds to heat transfer. This causes insufficient temperature difference between heated and cooled working fluid and reduces indicated work and efficiency. In the literature, Ahmed et al. [18], Karabulut et al. [34], Xiao et al. [48], and Alfarawi et al. [49] obtained similar results.

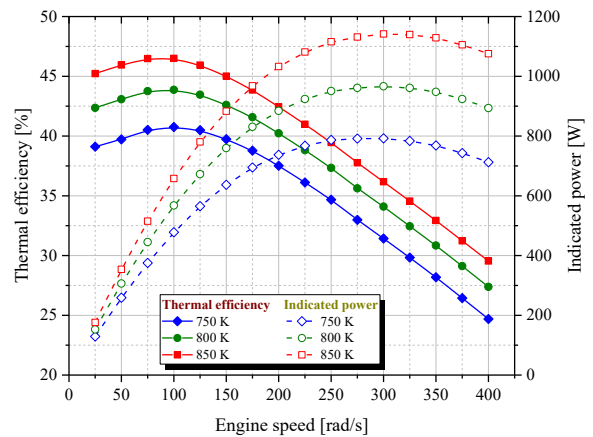


Fig. 14. The effect of the engine speed on the indicated power and thermal efficiency

The effect of the engine speed on the P-V diagram is given in Fig. 15. As indicated in the figure, the indicated work at 300 rad/s is less than that of the 100 rad/s. The duration of the cycle decreases due to the increase in the engine speed. Because of this, the heat transfer in the heating-cooling processes during the cycle period cannot occur sufficiently due to inadequate time.

When Figs. 14 and 15 are evaluated together, it can be realized that the indicated engine power increases when the engine speed increases from 100 rad/s to 300 rad/s although the work decreases. The power is identified as the work done per unit time (see Eq. (9)). For this reason, although the work done in each cycle decreases, it may increase depending on the number of cycles per second.

$$Power [W] = \frac{Work [J] \cdot Speed [rad/s]}{2\pi} \quad (9)$$

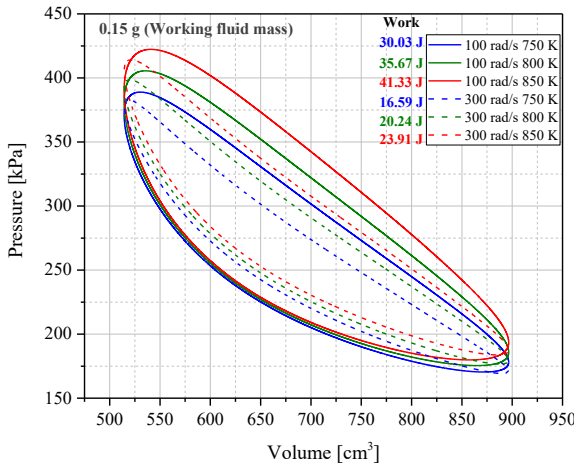


Fig. 15. The effect of the engine speed and hot-end temperature on the P-V diagram

2.3 The Effect of Displacer Height

Figs. 16 and 17 depict the effect of displacer height on the engine performance at different hot-end temperatures.

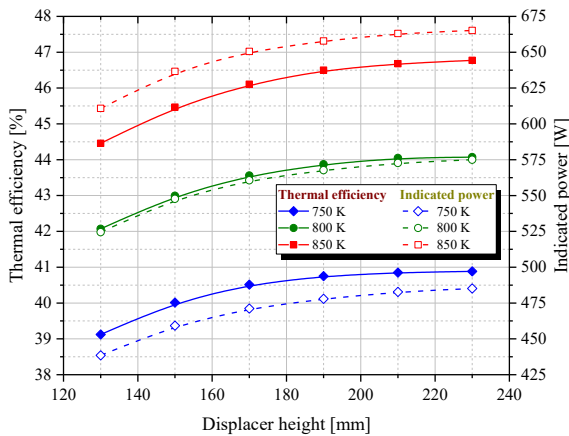


Fig. 16. The effect of the displacer height on the indicated power and thermal efficiency

As illustrated in Fig. 16, the increment in both the thermal efficiency and indicated power varies depending on the increase in the displacer height. An external regenerator was not used in this converted engine. Therefore, the regeneration process is provided by the working fluid passing through the heating-cooling channel between the cylinder wall and the displacer. Because of this, a higher displacer height provides a greater heat transfer area and improves power and efficiency. However, as demonstrated in the figure, the effect of this parameter becomes low as the height increases. In the literature,

similar results were also obtained by Raghavendra et al. [19], Bataineh [37], and Eid [50].

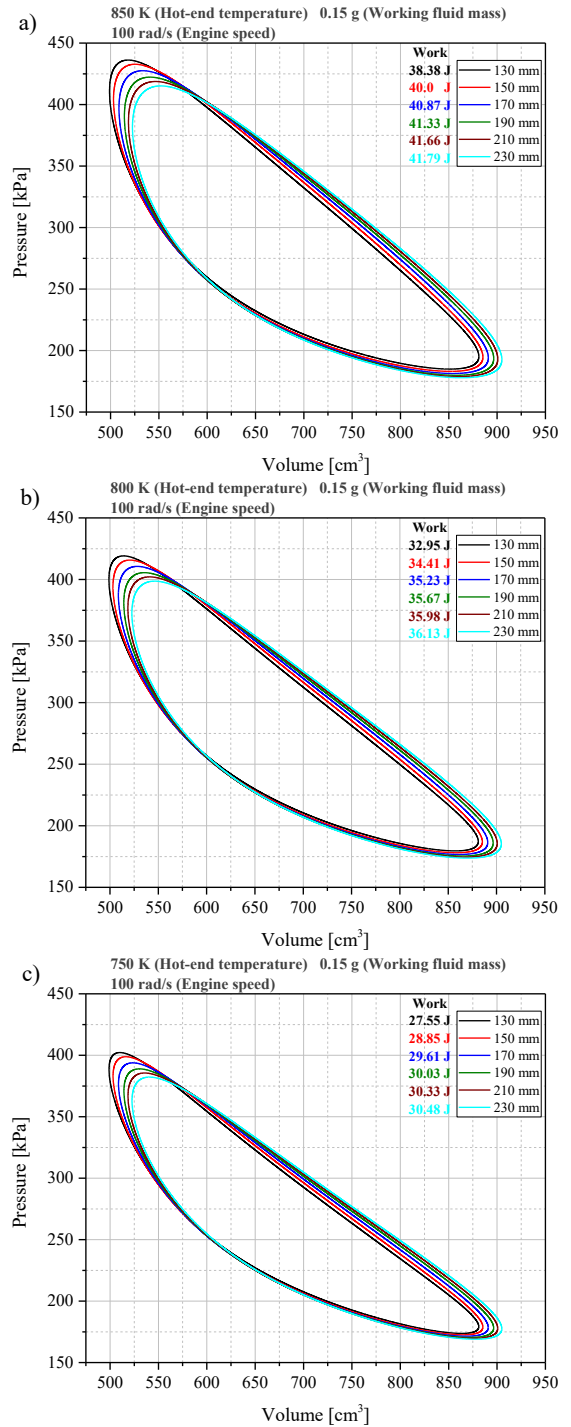


Fig. 17. The effect of the displacer height on the P-V diagram at hot-end temperatures: a) 850 K, b) 800 K, and c) 750 K

The variation of the indicated works depending on the displacer height for each hot-end temperature

is demonstrated in Fig. 17. It can be seen that the minimum and maximum values of the total volume increase based on displacer height. The swept volume remains constant since the crankshaft radius does not change. Only, the working fluid circulates between larger volumes because of the increasing displacer cylinder volume. The indicated work increases because of a greater heat transfer area. However, if the displacer height is increased more, the amount of improvement in the indicated work decreases. According to the literature [17], [18], [37], and [50], an increase in the dead volume has a negative effect on engine performance. Therefore, the volume of the regenerator should be large enough for good thermal capacity and engine output power.

If the results obtained for different displacer heights are compared with each other, it can be seen that when the displacer height increases from 130 mm to 190 mm, at 750 K, 800 K, and 850 K, the indicated work increases by 9 %, 8.25 %, and 7.7 %, respectively. However, when the size is increased from 190 mm to 230 mm, the increments are about 1.5 %, 1.3 %, and 1.1 %, respectively. Depending on the increase in the displacer height, the approaching of the indicated work to the isothermal work may also cause these results. The optimum displacer height was determined as 190 mm due to the decrease in the positive effect of the increase in the displacer height and the losses that would occur in the practical operation.

3 CONCLUSIONS

In this study, a double-cylinder V-type air compressor was converted to a γ -type Stirling engine. The block, cylinders, connecting rods, and crank mechanism of the air compressor constituted the main structure of the converted engine. However, a new piston, displacer, displacer cylinder, and other equipment were needed to form the converted engine. After this conversion, this study aimed to determine the optimum operating parameters of the Stirling engine for use in solar energy applications. For this purpose, the nodal thermodynamic analysis of the γ -type Stirling engine was conducted. Helium was considered as the working fluid due to its suitable thermodynamic properties and safety usage.

The optimum value of the working fluid mass and engine speed were determined as 0.15 g and 100 rad/s for all hot-end temperatures (750 K, 800 K, and 850 K). Also, the optimum displacer height was preferred as 190 mm since there was no significant improvement in the thermal efficiency

for the longer dimensions. By using these optimum values, the maximum thermal efficiency was obtained as 46.5 % (at 0.15 g working fluid mass, 100 rad/s engine speed, 190 mm displacer height, and 850 K hot-end temperature). At this operating condition, the indicated power was obtained as 657.8 W. The maximum indicated power was found as 1141.5 W at 300 rad/s (other parameters remained the same), but the thermal efficiency decreased to 36.2 % under this operating condition. It can be concluded that the thermal efficiency can be increased by optimizing the operating parameters of the Stirling engine.

4 REFERENCES

- [1] Ferreira, A.C., Silva, J., Teixeira, S., Teixeira, J.C., Nebra, S.A. (2020). Assessment of the Stirling engine performance comparing two renewable energy sources: Solar energy and biomass. *Renewable Energy*, vol. 154, p. 581-597, DOI:10.1016/j.renene.2020.03.020.
- [2] Laazaar, K., Boutammachte, N. (2020). New approach of decision support method for Stirling engine type choice towards a better exploitation of renewable energies. *Energy Conversion and Management*, vol. 223, 113326, DOI:10.1016/j.enconman.2020.113326.
- [3] Urciuolo, M., Chirone, R., Marra, F.S., Solimene, R. (2019). Power generation by Stirling engine during fluidized bed combustion of wood pellets. *Combustion Science and Technology*, vol. 191, no. 2, p. 263-274, DOI:10.1080/00102202.2018.1453122.
- [4] Singh, U.R., Kumar, A. (2018). Review on solar Stirling engine: Development and performance. *Thermal Science and Engineering Progress*, vol. 8, p. 244-256, DOI:10.1016/j.tsep.2018.08.016.
- [5] Strith, U., Zupan, G., Butala, V. (2007). A parametrical analysis of a biomass Stirling cogeneration unit for use in housing. *Strojniški vestnik - Journal of Mechanical Engineering*, vol. 53, no. 9, p. 556-568.
- [6] Karabulut, H., Okur, M., Cinar, C. (2022). Mechanical configuration and thermodynamic analysis of an alpha-type Stirling engine with crank-shifted driving mechanism. *Iranian Journal of Science and Technology, Transactions of Mechanical Engineering*, vol. 46, p. 431-448, DOI:10.1007/s40997-021-00436-2.
- [7] Abuelyamen, A., Ben-Mansour, R. (2018). Energy efficiency comparison of Stirling engine types (α , β , and γ) using detailed CFD modeling. *International Journal of Thermal Sciences*, vol. 132, p. 411-423, DOI:10.1016/j.ijthermalsci.2018.06.026.
- [8] Aksoy, F., Solmaz, H., Karabulut, H., Cinar, C., Ozgoren, Y.O., Polat, S. (2016). A thermodynamic approach to compare the performance of rhombic-drive and crank-drive mechanisms for a beta-type Stirling engine. *Applied Thermal Engineering*, vol. 93, p. 359-367, DOI:10.1016/j.applthermaleng.2015.09.105.
- [9] Shendage, D.J., Kedare, S.B., Bapat, S.L. (2011). An analysis of beta type Stirling engine with rhombic drive mechanism. *Renewable Energy*, vol. 36, no. 1, p. 289-297, DOI:10.1016/j.renene.2010.06.041.

- [10] Liu, M., Zhang, B., Zheng, K., Du, X., Wang, H. (2022). Numerical study on regenerative effectiveness of parallel-plate regenerator for Stirling engine. *International Journal of Green Energy*, vol. 19, no. 12, p. 1345-1356, DOI:10.1080/15435075.2021.1997750.
- [11] Malik, M.Z., Shaikh, P.H., Zhang, S., Lashari, A.A., Leghari, Z.H., Baloch, M.H., Memon, Z.A., Caiming, C. (2022). A review on design parameters and specifications of parabolic solar dish Stirling systems and their applications. *Energy Reports*, vol. 8, p. 4128-4155, DOI:10.1016/j.egy.2022.03.031.
- [12] Qiu, H., Wang, K., Yu, P., Ni, M., Xiao, G. (2021). A third-order numerical model and transient characterization of a b-type Stirling engine. *Energy*, vol. 222, 119973, DOI:10.1016/j.energy.2021.119973.
- [13] Cheng, C.H., Yu, Y.J. (2010). Numerical model for predicting thermodynamic cycle and thermal efficiency of a beta-type Stirling engine with rhombic-drive mechanism. *Renewable Energy*, vol. 35, no. 11, p. 2590-2601, DOI:10.1016/j.renene.2010.04.002.
- [14] Karabulut, H., Çınar, C., Öztürk, E., Yücesu, H.S. (2010). Torque and power characteristics of a helium charged Stirling engine with a lever controlled displacer driving mechanism. *Renewable Energy*, vol. 35, no. 1, p. 138-143, DOI:10.1016/j.renene.2009.04.023.
- [15] Cheng, C.H., Yang, H.S. (2012). Optimization of geometrical parameters for Stirling engines based on theoretical analysis. *Applied Energy*, vol. 92, p. 395-405, DOI:10.1016/j.apenergy.2011.11.046.
- [16] Topgül, T., Okur, M., Şahin, F., Çınar, C. (2022). Experimental investigation of the effects of hot-end and cold-end connection on the performance of a gamma type Stirling engine. *Engineering Science and Technology, an International Journal*, vol. 36, 101152, DOI:10.1016/j.jestch.2022.101152.
- [17] Kongtragool, B., Wongwiset, S. (2006). Thermodynamic analysis of a Stirling engine including dead volumes of hot space, cold space and regenerator. *Renewable Energy*, vol. 31, no. 3, p. 345-359, DOI:10.1016/j.renene.2005.03.012.
- [18] Ahmed, F., Zhu, S., Yu, G., Luo, E. (2022). A potent numerical model coupled with multi-objective NSGA-II algorithm for the optimal design of Stirling engine. *Energy*, vol. 247, 123468, DOI:10.1016/j.energy.2022.123468.
- [19] Raghavendra, H., Raju, P.S., Reddy, K.H. (2022). Effect of geometric and operational parameters on the performance of a beta-type Stirling engine: A numerical study. *Iranian Journal of Science and Technology, Transactions of Mechanical Engineering*, vol. 46, p. 1-13, DOI:10.1007/s40997-020-00406-0.
- [20] Ahmed, F., Hulin, H., Khan, A.M. (2019). Numerical modeling and optimization of beta-type Stirling engine. *Applied Thermal Engineering*, vol. 149, p. 385-400, DOI:10.1016/j.applthermaleng.2018.12.003.
- [21] Aksoy, F., Karabulut, H., Çınar, C., Solmaz, H., Özgören, Y.Ö., Uyumaz, A. (2015). Thermal performance of a Stirling engine powered by a solar simulator. *Applied Thermal Engineering*, vol. 86, p. 161-167, DOI:10.1016/j.applthermaleng.2015.04.047.
- [22] Cavallaro, F., Zavadskas, E.K., Streimikiene, D., Mardani, A. (2019). Assessment of concentrated solar power (CSP) technologies based on a modified intuitionistic fuzzy topsis and trigonometric entropy weights. *Technological Forecasting and Social Change*, vol. 140, p. 258-270, DOI:10.1016/j.techfore.2018.12.009.
- [23] Sharma, A. (2011). A comprehensive study of solar power in India and world. *Renewable and Sustainable Energy Reviews*, vol. 15, no. 4, p. 1767-1776, DOI:10.1016/j.rser.2010.12.017.
- [24] Kumar, A., Sharma, M., Thakur, P., Thakur, V.K., Rahatekar, S.S., Kumar, R. (2020). A review on exergy analysis of solar parabolic collectors. *Solar Energy*, vol. 197, p. 411-432, DOI:10.1016/j.solener.2020.01.025.
- [25] Zhu, J., Wang, K., Li, G., Wu, H., Jiang, Z., Lin, F., Li, Y. (2016). Experimental study of the energy and exergy performance for a pressurized volumetric solar receiver. *Applied Thermal Engineering*, vol. 104, p. 212-221, DOI:10.1016/j.applthermaleng.2016.05.075.
- [26] Zayed, M.E., Zhao, J., Li, W., Elsheikh, A.H., Zhao, Z., Khalil, A., Li, H. (2020). Performance prediction and techno-economic analysis of solar dish/stirling system for electricity generation. *Applied Thermal Engineering*, vol. 164, 114427, DOI:10.1016/j.applthermaleng.2019.114427.
- [27] Hijazi, H., Mokhiamar, O., Elsamni, O. (2016). Mechanical design of a low cost parabolic solar dish concentrator. *Alexandria Engineering Journal*, vol. 55, no. 1, p. 1-11, DOI:10.1016/j.aej.2016.01.028.
- [28] Shufat, S.A., Kurt, E., Cinar, C., Aksoy, F., Hançerlioğulları, A., Solmaz, H. (2019). Exploration of a Stirling engine and generator combination for air and helium media. *Applied Thermal Engineering*, vol. 150, p. 738-749, DOI:10.1016/j.applthermaleng.2019.01.053.
- [29] Kentfield, J.A.C. (1992). The thermodynamics of Stirling engines revisited: The relative merits of hot zone or cold zone work extraction. *SAE Technical Paper*, 929026, DOI:10.4271/929026.
- [30] Cinar, C., Yucesu, S., Topgul, T., Okur, M. (2005). Beta-type Stirling engine operating at atmospheric pressure. *Applied Energy*, vol. 81, no. 4, p. 351-357, DOI:10.1016/j.apenergy.2004.08.004.
- [31] Chahartaghi M., Sheykhi M. (2019). Energy, environmental and economic evaluations of a CCHP system driven by Stirling engine with helium and hydrogen as working gases. *Energy*, vol. 174, p. 1251-1266, DOI:10.1016/j.energy.2019.03.012.
- [32] Ben-Mansour, R., Abuelyamen, A., Mokheimer, E.M.A. (2017). CFD analysis of radiation impact on Stirling engine performance. *Energy Conversion and Management*, vol. 152, p. 354-365, DOI:10.1016/j.enconman.2017.09.056.
- [33] Cheng, C.H., Yang, H.S., Keong, L. (2013). Theoretical and experimental study of a 300-W beta-type Stirling engine. *Energy*, vol. 59, p. 590-599, DOI:10.1016/j.energy.2013.06.060.
- [34] Karabulut, H., Düzgün, M., Topgül, T. (2023). Nodal thermodynamic analysis of a three-cylinder gamma-type Stirling engine and a conventional gamma-type Stirling engine and performance comparison. *Journal of the Faculty of Engineering and Architecture of Gazi University*, vol. 38, no. 1, p. 45-56, DOI:10.17341/gazimmfd.944333.
- [35] İpci, D. (2021). Thermodynamic analysis of a gamma-type Stirling engine driven by Scotch Yoke mechanism. *International*

- Journal of Green Energy*, vol. 18, no. 2, p. 144-155, DOI:10.1080/15435075.2020.1831512.
- [36] Cinar, C., Ozdemir, A.O., Karabulut, H., Duzgun, M. (2021). Nodal thermodynamic and dynamic analysis of a free displacer Stirling engine. *Journal of Thermal Science and Technology*, vol. 41, no. 1, p. 141-155, DOI:10.47480/isibted.979390.
- [37] Bataineh, K.M. (2018). Numerical thermodynamic model of alpha-type Stirling engine. *Case Studies in Thermal Engineering*, vol. 12, p. 104-116, DOI:10.1016/j.csite.2018.03.010.
- [38] İpci, D., Karabulut, H. (2018). Thermodynamic and dynamic analysis of an alpha type Stirling engine and numerical treatment. *Energy Conversion and Management*, vol. 169, p. 34-44, DOI:10.1016/j.enconman.2018.05.044.
- [39] Karabulut, H., Çınar, C., Aksoy, F., Solmaz, H., Özgören, Y.Ö., Arslan, M. (2016). Design and performance tests of a beta type rhombic driven stirling engine. *Journal of the Faculty of Engineering and Architecture of Gazi University*, vol. 31, no. 4, p. 879-888, DOI:10.17341/gazimmfd.278443.
- [40] Karabulut, H., Solmaz, H., Okur, M., Şahin, F. (2013). Dynamic and thermodynamic analysis of gamma type free-piston Stirling engine. *Journal of the Faculty of Engineering and Architecture of Gazi University*, vol. 28, no. 2, p. 265-273.
- [41] Nour, M., Kosaka, H., Bady, M., Sato, S., Abdel-Rahman, A.K. (2017). Combustion and emission characteristics of DI diesel engine fuelled by ethanol injected into the exhaust manifold. *Fuel Processing Technology*, vol. 164, p. 33-50, DOI:10.1016/j.fuproc.2017.04.018.
- [42] Karagöz, Y., Balci, Ö., Köten, H. (2019). Investigation of hydrogen usage on combustion characteristics and emissions of a spark ignition engine. *International Journal of Hydrogen Energy*, vol. 44, no. 27, p. 14243-14256, DOI:10.1016/j.ijhydene.2019.01.147.
- [43] Akcay, M., Yilmaz, I.T., Feyzioglu, A. (2021). The influence of hydrogen addition on the combustion characteristics of a common-rail CI engine fueled with waste cooking oil biodiesel/diesel blends. *Fuel Processing Technology*, vol. 223, 106999, DOI:10.1016/j.fuproc.2021.106999.
- [44] Huang, Y., He, X., Zhang, H., Wei, J., Sng, D.W.M. (2021). Spark ignition and stability limits of spray kerosene flames under subatmospheric pressure conditions. *Aerospace Science and Technology*, vol. 114, 106734, DOI:10.1016/j.ast.2021.106734.
- [45] Rocha, D.D., Radicchi, F.C., Lopes, G.S., Brunocilla, M.F., Gomes, P.C.F., Santos, N.D.S.A., Malaquias, A.C.T., Filho, F.A.R., Baêta, J.G.C. (2021). Study of the water injection control parameters on combustion performance of a spark-ignition engine. *Energy*, vol. 217, 119346, DOI:10.1016/j.energy.2020.119346.
- [46] Karabulut, H., Çınar, C., Topgül, T., Uysal, L.K. (2022, Ahead of Print). Combined dynamic and thermodynamic investigation of a crank-shifted alpha-type Stirling engine. *Arabian Journal for Science and Engineering*, DOI:10.1007/s13369-022-06980-6.
- [47] Karabulut, H., Okur, M., Ozdemir, A.O. (2019). Performance prediction of a Martini type of Stirling engine. *Energy Conversion and Management*, vol. 179, p. 1-12, DOI:10.1016/j.enconman.2018.10.059.
- [48] Xiao, G., Qiu, H., Wang, K., Wang, J. (2021). Working mechanism and characteristics of gas parcels in the Stirling cycle. *Energy*, vol. 229, 120708, DOI:10.1016/j.energy.2021.120708.
- [49] Alfarawi, S., Al-Dadah, R., Mahmoud, S. (2016). Enhanced thermodynamic modelling of a gamma-type Stirling engine. *Applied Thermal Engineering*, vol. 106, p. 1380-1390, DOI:10.1016/j.applthermaleng.2016.06.145.
- [50] Eid, E. (2009). Performance of a beta-configuration heat engine having a regenerative displacer. *Renewable Energy*, vol. 34, no. 11, p. 2404-2413, DOI:10.1016/j.renene.2009.03.016.